Journal of Materials Chemistry A

ROYAL SOCIETY OF CHEMISTRY

PAPER

View Article Online
View Journal

Cite this: DOI: 10.1039/d1ta01852c

Atomically-dispersed cobalt ions on polyphenol-derived nanocarbon layers to improve charge separation, hole storage, and catalytic activity of water-oxidation photoanodes†

Yuri Choi, ‡[ab] Sanghyun Bae, ‡[ab] Byeong-Su Kim *[c] and Jungki Ryu *[ab]

For efficient photoelectrochemical (PEC) water oxidation, tailorable modification of photoanodes with various functional layers is inevitably required to address the inherent limitations of the photoanodes. In this study, we report that N-doped graphene quantum dots derived from natural polyphenol tannic acid (N-TAGQDs) can form ultrathin and stable layers on a $BiVO_4$ photoanode together with Co^{2+} ions ($BiVO_4$/Co/N-TAGQD) by a simple dipping method and significantly improve PEC water-oxidation performance. A series of systematic analyses suggest the synergistic effect of graphitization of precursors to N-TAGQDs, N-doping, and the presence of phenolic groups to impart multifunctional roles of improving charge separation, hole storage, and catalytic activity. We believe that this simple method provides insights for the development of novel photoanodes and design of versatile carbon nanomaterials.

Received 3rd March 2021
Accepted 10th May 2021

DOI: 10.1039/d1ta01852c

rsc.li/materials-a

Introduction

Solar water oxidation is a practically important and academically intriguing photoelectrochemical (PEC) reaction for sustainable production of various chemicals.[1–3] Electrons extracted from water through a series of photophysical and interfacial electrochemical processes can be used to produce fuels and valuable chemicals through reduction reactions, such as hydrogen evolution,[3] CO_2 reduction,[4] nitrogen reduction,[5] and reductive enzyme reactions.[6] In principle, any semiconducting materials with a sufficiently large band gap and suitable band-edge positions can be used for solar water oxidation.[1–3] In this regard, n-type oxide semiconductors, such as Fe_2O_3,[7,8] $BiVO_4$,[9,10] and WO_3,[11,12] have been considered promising water-oxidation photoanodes due to their relatively high stability against oxidation. However, these oxide semiconductors have intrinsic limitations, including low extinction coefficient, severe recombination of photogenerated charge carriers, poor electrical conductivity, and low catalytic activity, resulting in poor efficiency of solar water oxidation.[2,7,10] Thus, the modification of photoanodes with various functional materials is inevitably required to enhance the efficiency of PEC reactions.[11–14]

In this context, nanocarbons, such as carbon dots (CDs), graphene quantum dots (GQDs), graphene (oxide), reduced graphene oxide, and carbon nitride, have drawn attention from researchers due to their unique and readily tunable optical and electrical properties.[14–20] For example, it is reported that CDs can be used as efficient visible light photosensitizers for solar water oxidation.[21–25] To date, nanocarbons have been popularly employed in a powder-type photocatalyst[21,22] but less in the fabrication of water-oxidation photoanodes.[23–29] However, even for the latter cases, an effective method of deposition on the desired photoanode substrates has been lacking. Conventional approaches, such as dipping, electrochemical deposition, and hydrothermal methods, without concerns regarding the adhesion mechanism, have resulted in the deposition of nonuniform nanocarbon layers with low efficiency and stability in PEC performance.[23–25] Moreover, the role of these nanocarbons has been mostly limited to that of a photosensitizer, requiring additional surface modification with a thick layer of oxygen evolution catalysts (OECs) for efficient solar water oxidation.[24,30]

Herein, we report the fabrication of ultrathin, uniform, and stable nanocarbon layers with multifunctional roles for efficient PEC water oxidation. Nontoxic and cost-effective nitrogen-doped GQDs with phenolic groups (N-TAGQDs) are hydrothermally synthesized from tannic acid (TA) for strong adhesion to the photoanode substrate with a concomitant accommodation of catalytically active Co^{2+} ions. A simple dipping method enables the deposition of 2.2 nm of ultrathin and uniform

[a]Department of Energy Engineering, School of Energy and Chemical Engineering, Ulsan National Institute of Science and Technology (UNIST), Ulsan 44919, Republic of Korea. E-mail: jryu@unist.ac.kr

[b]Emergent Hydrogen Technology R&D Center, Ulsan National Institute of Science and Technology (UNIST), Ulsan 44919, Republic of Korea

[c]Department of Chemistry, Yonsei University, Seoul 03722, Republic of Korea. E-mail: bskim19@yonsei.ac.kr

† Electronic supplementary information (ESI) available. See DOI: 10.1039/d1ta01852c

‡ Equal contribution.

layers of N-TAGQs and Co^{2+} ions on a model $BiVO_4$ photoanode ($BiVO_4$/Co/N-TAGQD) *via* the metal–ligand complexation, improving the PEC performance of the underlying $BiVO_4$ photoanodes considerably. A series of systematic studies with PEC and kinetic analyses suggest a synergistic effect of graphitization of GQD precursors, N-doping, and the presence of phenolic groups for efficient and stable solar water oxidation. It is found that the abundant functional groups, such as phenolic and pyrrolic nitrogen (N) groups, of N-TAGQDs act as metal coordination sites and are responsible for the formation of uniform and stable nanocarbon layers. Furthermore, the ultrathin Co/N-TAGQD layers significantly improve charge separation, hole storage, and catalytic efficiencies, enabling efficient PEC water oxidation by the underlying $BiVO_4$ photoanodes. This study can provide insights for the design and synthesis of versatile carbon nanomaterials toward efficient PEC devices.

Experimental section

Synthesis of nitrogen-doped graphene quantum dots (N-TAGQDs)

To prepare N-TAGQDs, 5 mg of TA and 20 μL of 2 M NaOH were dissolved in 10 mL of water under vigorous stirring. Then, 2 μL of ethylenediamine (0.03 mmol) was added to the solution, followed by a hydrothermal reaction at 180 °C for 6 h in a sealed Teflon-lined autoclave. After cooling to room temperature, the brown suspension was dialyzed (SpectraPore MWCO 1000) for 2 days to remove the salts and unreacted chemicals. In addition, non-doped TAGQDs was synthesized in the absence of ethylenediamine. For control experiment, we synthesized two types of nitrogen-doped CDs without phenolic groups such as N-CCDs and N-UCDs, as reported previously.[43]

Fabrication of $BiVO_4$ photoanode

The $BiVO_4$ was fabricated on a fluorine-doped tin oxide (FTO) substrate with a SnO_2 buffer layer to reduce recombination between the FTO and $BiVO_4$ interface. To prepare the Sn precursor solution, 0.1 M of $SnCl_2 \cdot 2H_2O$ was dissolved in isopropyl alcohol with stirring for 1 h and kept for 1 day under ambient conditions before use. The SnO_2 layer was deposited on an FTO substrate by the spin-coating method at 4500 rpm for 20 s and an annealing process under 500 °C for an hour.[51] Then, $BiVO_4$ was deposited by the metal–organic deposition method.[52] Briefly, 0.14 M of $VO(acac)_2$ in methanol with an aging time of 4 days was mixed with 0.5 M of $Bi(NO_3)_3 \cdot 5H_2O$ in acetic acid at a 1 : 1 of molar ratio of Bi/V. The mixed solution was deposited using the spin-coating method at 1500 rpm for 20 s, and the prepared substrate was annealed at 480 °C in a preheated muffle furnace for 30 min under air condition. The above process was carried out 4 times to obtain an appropriate thickness of $BiVO_4$.

Modification of $BiVO_4$ photoanode with Co ions and N-TAGQDs

The $BiVO_4$ electrode was dipped into 10 mM of cobalt nitrate solution for 1 h. The electrode was washed with water. Then, the $BiVO_4$/Co electrode was dipped into 0.5 mg mL^{-1} of N-TAGQD solution for 2 h. After washing with water several times, the $BiVO_4$/Co/N-TAGQD electrode was dried at 60 °C for 12 h. As the control sets, 0.5 mg mL^{-1} of TA, U-CCDs, N-UCDs, and TAGQDs were used instead of N-TAGQDs, respectively.

Characterizations

A UV/vis spectrophotometer (UV-2550, Shimadzu) was used to record the absorption spectra of N-TAGQDs. The HOMO level of N-TAGQDs was evaluated by UPS (ESCALAB 250XI, Thermo Fisher). The zeta-potential of the colloidal suspensions was measured using a zeta-potential analyzer (Malvern, Zetasizer nano-zs). The structure of N-TAGQDs was analyzed by FT-IR (Cary 660, Varian) and XPS (K-alpha, Thermo Fisher) spectroscopy. The band gap of $BiVO_4$/Co/N-TAGQD was analysed by XPS/UPS (ESCALAB 250XI, Thermo Fisher). The morphology of N-TAGQDs and $BiVO_4$/Co/N-TAGQD was examined using a SEM (S-4800, Hitachi High-Technologies), AFM (tapping mode; Veeco, Nanoscope V), high-resolution TEM, high-angle annular dark-field scanning TEM, and energy dispersive X-ray spectroscopy (JEOL, JEM-2100F, accelerating voltage of 200 kV).

PEC characterizations

PEC characterizations were carried out in a three-electrode configuration under back-side illumination. PEC measurements under illumination were conducted with a solar simulator (94023A, Newport) equipped with a 450 W Xe lamp and AM 1.5 G filter for class 3A. For the $BiVO_4$ photoanode, 0.1 M phosphate buffer (pH 7.0) was used as the electrolyte solution. A SP-150 Biologic potentiostat (BioLogic Science Instruments, France) was used to regulate the potential of the working electrode under the following conditions: $BiVO_4$ as the working electrode, Ag/AgCl as the reference electrode, Pt film as the counter electrode, and scan rates of 10 mV s^{-1}. The IPCE measurement was performed under monochromatic light by a light source 300 W Xe arc lamp equipped with a CD130 monochromator (Newport Corporation, CA, USA). EIS was measured by SP-150 (BioLogic Science Instruments, France) under illumination with the following conditions: applied bias of 0.6 V *vs.* RHE, amplitude of 20 mV, and frequency range from 0.1 Hz to 100 kHz. Numerical fitting of EIS data was conducted using EC-Lab software (BioLogic Science Instruments, France).

Determination of PEC efficiency

Injection efficiency and separation efficiency for evaluation of PEC efficiency in each photoelectrode were calculated by using the following equations.

$$\text{Injection efficiency (\%)} = J_{H_2O}/J_{Na_2SO_3} \quad (1)$$

$$\text{Separation efficiency (\%)} = J_{Na_2SO_3}/(J_{Max} \times \eta_{Abs}) \quad (2)$$

where $J_{Na_2SO_3}$ and J_{H_2O} are photocurrent densities obtained under PEC water oxidation condition with and without an electron donor, respectively. J_{Max} is the theoretical photocurrent

density calculated by the solar photon flux, and η_{Abs} is the absorption efficiency of each photoelectrode.

The open-circuit potential (OCP) measurement was carried out to determine photovoltage and carrier lifetime in photoelectrodes. Photovoltage was estimated by the OCP gap under dark and light conditions, and the lifetime of electrons was calculated by using following equation with the decay in the OCP curve.

$$\tau = -\frac{kT}{e}\left(\frac{\mathrm{dOCP}}{\mathrm{d}t}\right)^{-1} \quad (3)$$

where τ is the electron lifetime, kT is the thermal energy, and e is the positive elementary charge.

The ratio of the hole accumulation and recombination (A/R) was calculated from the integral values of positive (PT) and negative (NT) transient spikes.

$$\text{Hole A/R ratio} = C_{PT}/C_{NT} \quad (4)$$

where C_{PT} and C_{NT} are charge carrier densities obtained in the chopped chronoamperometry measurement under PEC water oxidation at 0.6 V *vs.* RHE. C_{PT} and C_{NT} indicate accumulation of holes in semiconductor surface and back recombination of bulk electrons and accumulated holes.

Results and discussion

Design of nanocarbon layers with Co^{2+} ions

For the uniform and stable deposition of multifunctional GQDs on a model $BiVO_4$ photoanode, we synthesized GQDs through a hydrothermal method using TA and ethylenediamine as precursors (Scheme 1a). In previous studies, various GQDs were deposited on the desired photoelectrodes for improved light absorption or charge separation in PEC systems by dip-coating, electrodeposition, and direct hydrothermal synthesis.[23–25] In general, however, these previous studies have the following limitations: no detailed adhesion mechanism of GQDs suggested, nonuniform deposition of GQDs, low PEC performance, limited stability, and requirement of additional modification with OECs. To address these issues and impart multifunctionality to GQDs for efficient PEC water oxidation, we chose TA with abundant phenolic groups, which have a strong adhesion property to the substrate, as GQDs precursor. In addition, ethylenediamine was introduced as the N-doping source. It is expected that N-TAGQDs can be uniformly deposited on $BiVO_4$ photoanodes and have multifunctional roles desirable for efficient PEC water oxidation (Scheme 1b). Although GQDs are generally highly soluble[31] and thus can be readily detached from the underlying photoelectrodes in aqueous solution, N-TAGQDs can strongly bind to the photoelectrodes by forming a stable metal–polyphenol complex.[32–35] Additionally, considering that free polyphenol groups in N-TAGQDs can accommodate metal ions such as Co^{2+} and form a ligand-to-metal charge-transfer (LMCT) complex,[34,35] one can expect that N-TAGQDs bearing Co^{2+} ions can further enhance the catalytic activity[36–39] of the underlying photoanodes for solar water oxidation.

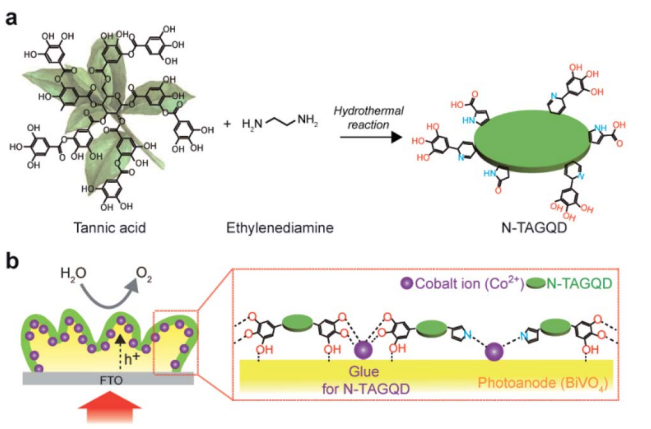

Scheme 1 Schematic illustrations of the synthesis and application of N-TAGQDs for PEC water oxidation. (a) Hydrothermal synthesis of N-TAGQDs using TA and ethylenediamine. (b) Deposition of N-TAGQDs with Co^{2+} ions on the surface of photoanodes by metal–ligand complexation for PEC water oxidation.

Before deposition, as-synthesized N-TAGQDs were characterized by transmission electron microscopy (TEM), atomic force microscopy (AFM), and various spectroscopies. In accordance with the dynamic light scattering diagram (Fig. S1†), N-TAGQDs were approximately 11 nm in diameter with a lattice spacing of 0.36 nm, which matched with (002) facets of graphite (Fig. 1a), and ~1.1 nm in thickness (Fig. S2†). N-TAGQDs showed a strong absorption peak at 260 nm and a broad band above 400 nm due to sp^2-carbon network and surface states, respectively (Fig. S3a†).[31] According to the Tauc plot and ultraviolet photoelectron spectroscopy (UPS) analyses, N-TAGQDs had a bandgap of 3.07 eV with the HOMO level (2.54 V *vs.* RHE) more positive than the redox potential of water oxidation (1.23 V *vs.* RHE) (Fig. S3b and c†). High-resolution C 1s, N 1s, and O 1s X-ray photoelectron spectroscopy (XPS) showed that N-TAGQDs had high contents of (1) carboxylic acid, which was in accordance with the negative zeta-potential of N-TAGQDs (−35 ± 0.6 mV); (2) pyrrolic N (59% among various C–N configurations); and (3) phenolic groups, respectively (Fig. 1b). Fourier-transform infrared (FT-IR) spectroscopy also confirmed that phenolic groups from TA still remained in N-TAGQDs after the hydrothermal reaction (Fig. S4†). To identify potential binding sites for the deposition on photoanodes and accommodation of metal ions, we carried out XPS analysis of N-TAGQD samples with and without exposure to Co^{2+} ions at pH 7 (Fig. S5†). After the exposure, the ratio of carboxylic, phenolic, and pyrrolic N groups was reduced, with a noticeable shift of phenolate-related peaks from 531.5 to 532.5 eV. These results suggest that although various functional groups can form a metal–ligand complex, phenolic groups form the strongest interactions in N-TAGQDs.[40]

Based on these results, we attempted to deposit N-TAGQDs on $BiVO_4$ photoanodes by a simple dipping method. To improve the adhesion stability of N-TAGQDs and impart catalytic activity for water oxidation, $BiVO_4$ photoanodes were treated with Co^{2+} ions and then coated with N-TAGQDs ($BiVO_4$/Co/N-TAGQD). Note that $BiVO_4$ photoanodes were exposed to

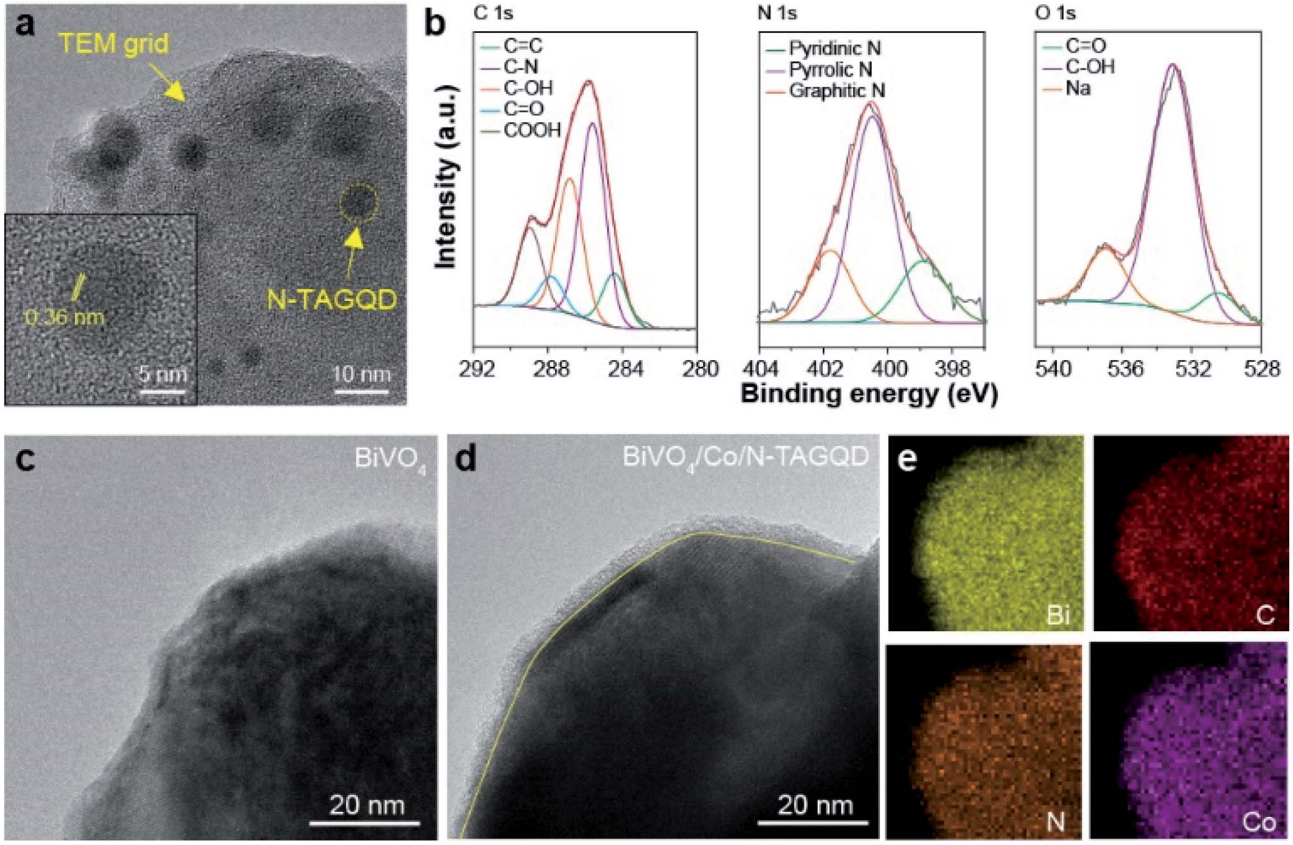

Fig. 1 Characterization of as-synthesized N-TAGQDs and nanocarbon layers assembled from Co^{2+} ions and N-TAGQDs on $BiVO_4$ ($BiVO_4$/Co/N-TAGQD). (a) A TEM image of N-TAGQDs. (Inset) A high-resolution TEM image of N-TAGQDs. (b) High-resolution C 1s, N 1s, and O 1s XPS spectra of N-TAGQDs. (c and d) TEM images of (c) bare $BiVO_4$ and (d) $BiVO_4$/Co/N-TAGQD photoanodes. (e) Elemental mapping analysis of $BiVO_4$/Co/N-TAGQD in (d). The yellow line in (d) indicates the nanocarbon layers on $BiVO_4$ electrode.

Co^{2+} prior to N-TAGQDs to avoid the potential detachment of N-TAGQDs by Co^{2+} ions in solution. As control groups, we also prepared $BiVO_4$ photoanodes treated only with N-TAGQDs ($BiVO_4$/N-TAGQD) or Co^{2+} ions ($BiVO_4$/Co), respectively. Compared with bare $BiVO_4$, there was a slight increase of absorbance from 300 to 450 nm after the treatment with Co^{2+} alone, N-TAGQDs alone, and both of them, implying their deposition (Fig. S6†). For all samples except for $BiVO_4$/Co/N-TAGQD, however, both scanning electron microscopy (SEM) and TEM analyses showed no obvious morphological changes after the modification, possibly due to a low degree of loading, small size, and low contrast of each component (Fig. S7 and S8†). Interestingly, for $BiVO_4$/Co/N-TAGQD, 2.2 nm of an ultrathin and uniform layer was observed on $BiVO_4$ in the TEM image, implying face-on deposition of N-TAGQDs (Fig. 1c and d).[41] Elemental mapping analysis by energy-dispersive X-ray spectroscopy indicated a homogeneous distribution of the respective elements (*i.e.*, C, N and Co) in $BiVO_4$/Co/N-TAGQD photoanodes (Fig. 1e). These results suggest that the deposition of Co^{2+} ions provides additional glue for the deposition of uniform and stable N-TAGQD layers on $BiVO_4$ photoanodes. Co 2p XPS spectrum of $BiVO_4$/Co/NTAGQD was consistent with that of atomically dispersed Co^{2+} on N-doped nanocarbons reported previously (Fig. S9†).[42]

PEC performance of $BiVO_4$ modified with nanocarbons and Co^{2+} ions

To evaluate the effect of the ultrathin N-TAGQD layers with Co^{2+} ions on the performance of the underlying $BiVO_4$ photoanodes (Fig. 2a), PEC analyses were carried out in 0.10 M phosphate buffer at pH 7.0 under simulated sunlight illumination. Fig. 2b shows the linear sweep voltammetry (LSV) curves of pristine $BiVO_4$, $BiVO_4$/N-TAGQD, $BiVO_4$/Co, and $BiVO_4$/Co/N-TAGQD photoanodes. Whereas $BiVO_4$/N-TAGQD exhibited slight improvements of the photocurrent density and onset potential for water oxidation, $BiVO_4$/Co exhibited considerably improved onset potential (from 0.65 to 0.31 V *vs.* RHE) with a moderate increase of photocurrent density. These results indicate the OEC activity of the deposited Co^{2+} ions. On the contrary, $BiVO_4$/Co/N-TAGQD showed both a large cathodic shift of onset potential to 0.21 V *vs.* RHE and a significantly increased photocurrent density (2.75 mA cm^{-2}). In addition, $BiVO_4$/Co/N-TAGQD exhibited a negligible performance degradation (<5% in terms of photocurrent density at 1.23 V *vs.* RHE) after 2 h under intermittent irradiation, whereas $BiVO_4$/Co experienced a rapid performance degradation, possibly due to dissociation of Co^{2+} (Fig. 2c). There was no noticeable delamination of the Co/N-TAGQD layers from the underlying $BiVO_4$ (Fig. S9 and S10†).

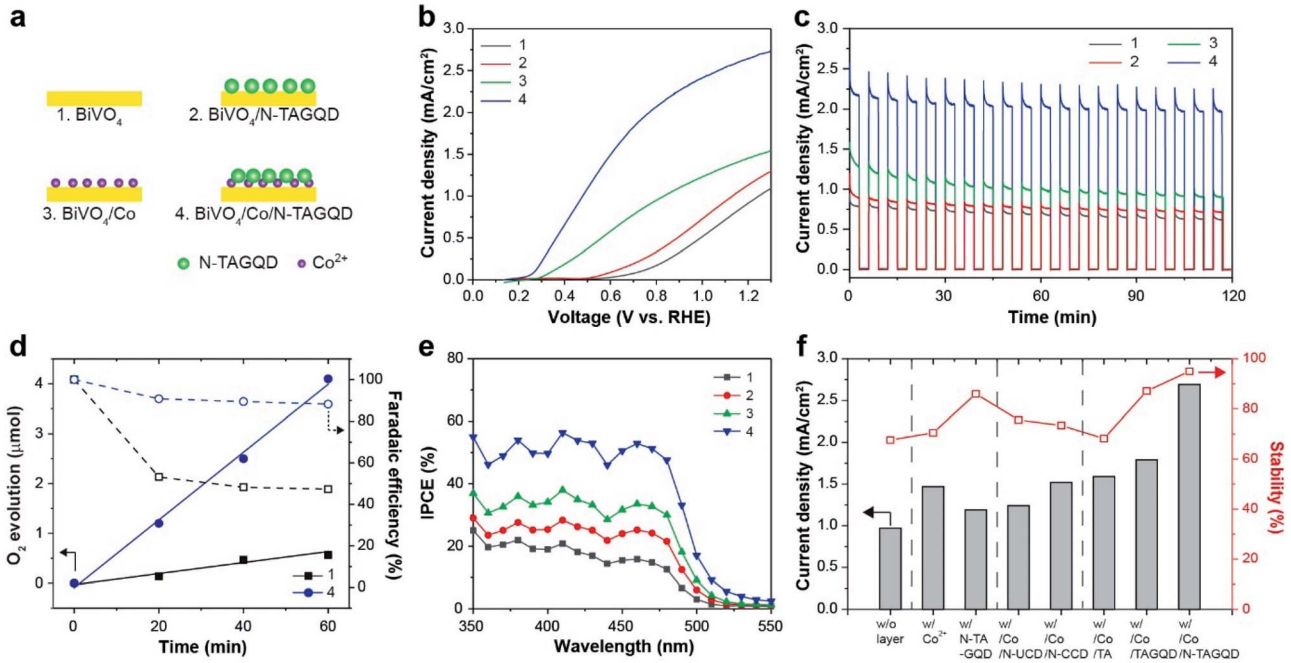

Fig. 2 Effect of the Co/N-TAGQD layers on the PEC performance of $BiVO_4$ photoanodes. (a) Schematic representative photoanodes of (1) $BiVO_4$, (2) $BiVO_4$/N-TAGQD, (3) $BiVO_4$/Co, and (4) $BiVO_4$/Co/N-TAGQD. (b) LSV curves of the respective photoanodes under the simulated solar irradiation. Scan rate: 10 mV s^{-1}. (c) Chronoamperograms of the respective photoanodes at 1.23 V *vs.* RHE with chopped light. (d) O_2 gas evolution profiles of bare (1) $BiVO_4$ and (4) $BiVO_4$/Co/N-TAGQD at 1.23 V *vs.* RHE under continuous light. (e) IPCE spectra of the respective photoanodes at 1.23 V *vs.* RHE. (f) Comparison of photocurrent density and stability at 1.23 V *vs.* RHE.

These results suggest high electrochemical and adhesion stability of the Co/N-TAGQD layers, as expected. Both gas chromatography (Fig. 2d) and incident photon-to-current conversion efficiency (IPCE) (Fig. 2e) analyses confirmed highly improved PEC performance of $BiVO_4$ photoanodes due to the Co/N-TAGQD layers. The faradaic efficiencies of $BiVO_4$ and $BiVO_4$/Co/N-TAGQD were 47% and 88%, respectively, after 1 h at 1.23 V *vs.* RHE under continuous irradiation. It is noteworthy here that IPCE was considerably improved even with only N-TAGQD layers over the entire absorption range of $BiVO_4$. Considering that N-TAGQD layers have a negligible contribution to light absorption (Fig. S6†) and poor catalytic activity for water oxidation, the IPCE measurement suggests that N-TAGQDs can play additional roles in efficient PEC water oxidation.

To clarify the role of phenolic groups and N-doping on the multifunctional N-TAGQDs, we prepared other control sets for comparison: (1) TAGQDs without N-doping and (2) N-doped carbon dots without phenolic groups (Fig. S11–S13†). Especially, citric acid and urea were used as carbon sources to prepare N-doped carbon dots without phenolic groups (N-CCD and N-UCD, respectively).[43] These CDs were deposited on $BiVO_4$ together with Co^{2+} ions. In addition, a precursor TA was deposited with Co^{2+} because it was previously reported that metal–TA complexes displayed excellent electrocatalytic activity for water oxidation.[36,39] Unlike $BiVO_4$/Co/N-TAGQD, aggregated particles and non-uniform thick layer were observed for $BiVO_4$/Co/N-UCD, $BiVO_4$/Co/N-CCD, and $BiVO_4$/Co/TA (Fig. S11†). Through these comparative analyses (Fig. S12 and S13†), we found that both N-doping and phenolic groups play an important role in the PEC process for solar water oxidation (Fig. 2f). First, N-TAGQDs were more efficient than non-doped TAGQDs in enhancing the PEC performance of $BiVO_4$ photoanodes. Second, nanocarbons with phenolic groups (*i.e.*, TAGQDs and N-TAGQDs) had higher stability than those without them (*i.e.*, N-CCDs and N-UCDs). Whereas the former exhibited only a slight photocurrent decrease during chronoamperometric analysis, the latter showed a rapid and significant photocurrent reduction, suggesting critical roles of phenolic groups in the formation of robust nanocarbon layers with higher stability

Table 1 The fitting parameters obtained from EIS analysis in Fig. 3a

No.	Photoanode	R_s (Ω cm^{-2})	C_{sc} (F cm^{-2})	R_{bulk} (Ω cm^{-2})	C_{ss} (F cm^{-2})	R_{ct} (Ω cm^{-2})
1	$BiVO_4$	55.38	1.77×10^{-5}	355.4	8.50×10^{-5}	5651
2	$BiVO_4$/N-TAGQD	49.19	1.39×10^{-5}	269.6	1.14×10^{-4}	3929
3	$BiVO_4$/Co	50.01	1.50×10^{-5}	245.9	8.55×10^{-5}	912
4	$BiVO_4$/Co/N-TAGQD	42.86	5.40×10^{-6}	121.6	6.70×10^{-4}	181

(Fig. 2f). Lastly, although N-TAGQDs exhibited the best performance in terms of both performance and stability, TAGQDs were much more efficient than their precursor TA. According to the literature, metal–TA complexes have a low PEC efficiency and stability due to weak coordination of TA with metal in phosphate electrolytes (pH 7).[44] Thus, the high activity and stability of the Co/N-TAGQD layer can be attributed to more abundant phenolic groups per unit and the presence of additional functional groups for complex formation, such as carboxylic acids and pyrrolic N groups, as discussed earlier in XPS analysis. These results suggest the synergistic effect of graphitization of GQD precursors, N-doping, and presence of phenolic groups on the observed performance improvement of $BiVO_4$ photoanodes by the ultrathin Co/N-TAGQD layers.

(Photo)electrochemical analysis to evaluate charge carrier kinetics

To elucidate the underlying mechanism for the significantly improved PEC performance of $BiVO_4$ photoanodes by the ultrathin Co/N-TAGQD layers, the photogenerated charge-carrier kinetics were investigated through electrochemical impedance spectroscopy (EIS). The measured Nyquist plots were fitted using a two-RC equivalent circuit, which was composed of the space-charge capacitance (C_{sc}) of bulk $BiVO_4$, carrier migration resistance (R_{bulk}) from the bulk $BiVO_4$, surface-state capacitance (C_{ss}) associated with charge separation, and charge transfer resistance (R_{ct}) by the electrochemical reactions at the photoanode-electrolyte interface (Tables 1, S1, Fig. 3a and S14†).[7,23,24] To better understand the frequency-dependent PEC kinetics, Bode plots were also compared and deconvoluted to high- and low-frequency components, which can be correlated to the rate of rapid charge transport process in the bulk photoanode and slow catalytic reaction at the photoanode-electrolyte interface, respectively (Fig. 3b and Table S2†).[10,45] Our results suggest the roles of Co^{2+} ions and N-TAGQDs in enhancing the catalytic activity and charge transport/separation efficiency of $BiVO_4$ photoanodes, respectively. Note that the former (or the latter) can be deduced from the decrease of R_{ct} (or R_{bulk}/C_{sc}) in the Nyquist plot and a shift of low-frequency (or high-frequency) component to a higher frequency with a decrease of the corresponding phase angle.[10,45] These results were consistent with the measurement of the charge separation and injection efficiencies (Fig. 3c, S15 and S16†). In addition to such improvements, $BiVO_4$/Co/N-TAGQD exhibited a notable increase of C_{ss}, suggesting the storage of holes beneficial for more efficient PEC water oxidation.[7,46,47]

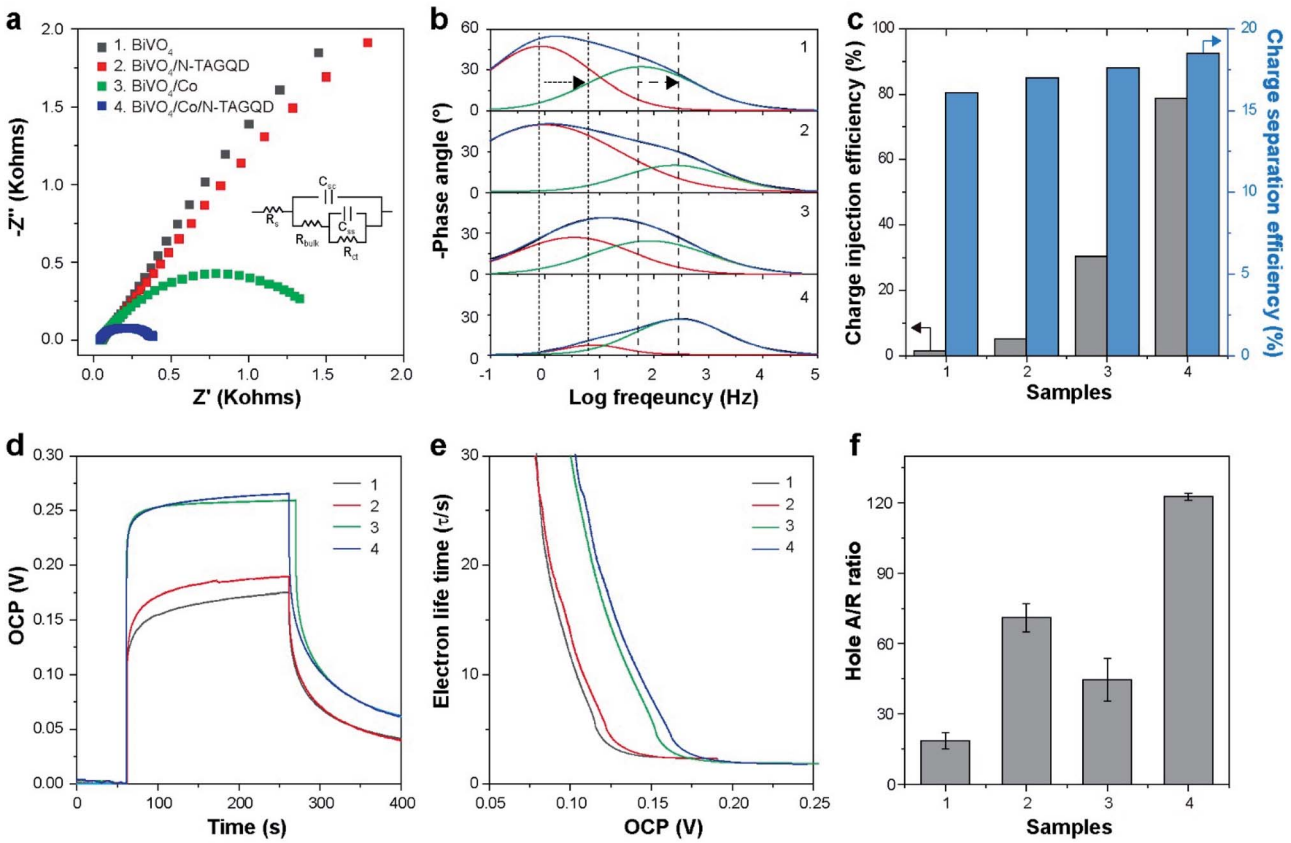

Fig. 3 Kinetic analysis showing the multifunctional roles of the Co/N-TAGQD layers in the improved PEC performance of the underlying $BiVO_4$ photoanodes. (a) Nyquist and (b) Bode plot analyses of (1) $BiVO_4$, (2) $BiVO_4$/N-TAGQD, (3) $BiVO_4$/Co, and (4) $BiVO_4$/Co/N-TAGQD photoanodes at 0.4 V *vs.* RHE. Inset shows an equivalent circuit. (c) Charge injection and separation efficiencies of the respective photoanodes at 0.6 V *vs.* RHE. (d) Open circuit potential (OCP) graph and (e) the lifetime of electrons calculated from the OCP graph. (f) The calculated ratios of the hole accumulation and recombination (A/R) in the respective photoanodes.

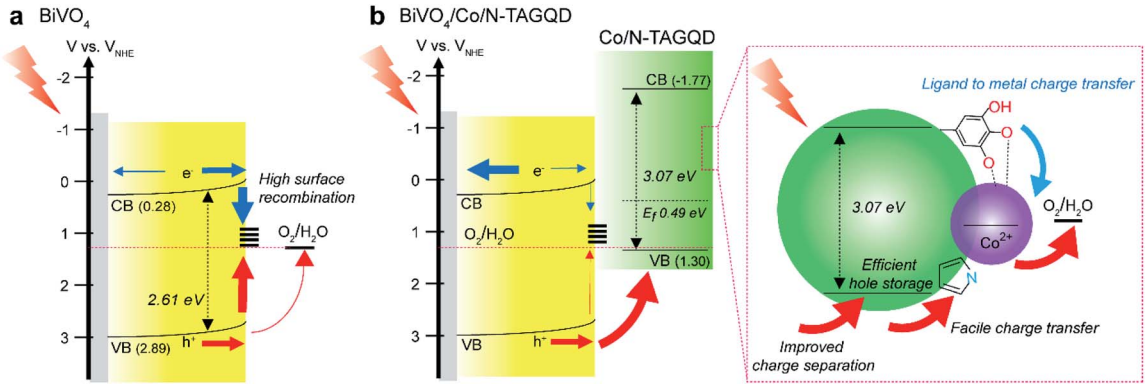

Scheme 2 Schematic illustration of the proposed mechanism of PEC water oxidation in (a) bare $BiVO_4$ and (b) $BiVO_4$/Co/N-TAGQD photoanodes.

Comparison with $BiVO_4$/Co/TA and $BiVO_4$/Co/N-TAGQD showed that the simultaneous graphitization to GQDs with N-doping significantly improves the catalytic charge transfer for water oxidation (Fig. S17 and Table S3†). Although both $BiVO_4$/Co/TA and $BiVO_4$/Co/TAGQD also improved the charge transport in the bulk, they resulted in a slight reduction of R_{ct} and a small shift of the low-frequency component. These results indicate that graphitized and N-doped GQDs can enhance the charge transfer between photoanodes and Co^{2+} ions, thereby improving photocatalytic activity for water oxidation. We assume that the superior properties of N-TAGQDs arise from a high population of diverse functional groups in N-TAGQDs including pyrrole N groups, which are known to enhance the electronegativity, catalytic activity, and charge transfer efficiency by the metal–nitrogen complex more effectively than other C–N configurations,[48] for the accommodation of Co^{2+} ions and enhanced OER efficiency.

To unveil the origin of the improved charge separation efficiency, we measured the open-circuit potential (OCP) and charge-carrier lifetimes of photoanodes before and after the modification with N-TAGQDs and Co^{2+} ions. The OCP value was increased from 0.165 V to 0.181 V and 0.259 V after modification with N-TAGQDs and Co/N-TAGQD, respectively (Fig. 3d). We found that charge-carrier lifetime was also increased at the same OCP values after modification of N-TAGQDs. Particularly, $BiVO_4$/Co/N-TAGQD showed the longest lifetime compared with other samples. We hypothesized that the increase of both OCP and charge-carrier lifetime could be attributed to the suppression of surface recombination centers[49,50] because it is reasonably anticipated that ultrathin Co/N-TAGQD layers have a negligible effect on the band structure of bulk $BiVO_4$. To confirm our hypothesis, we calculated the ratio between the accumulated and recombined holes (A/R ratio; Fig. 3f) using transient photocurrent-spike measurements (Fig. S18†). In general, the hole A/R ratio was considerably increased after the modification, confirming the suppression of surface recombination. Note that a lower hole A/R ratio for the $BiVO_4$/Co than for the $BiVO_4$/N-TAGQD can be ascribed to higher interfacial catalytic activity of the deposited Co^{2+} ions, as expected from the EIS analysis (Fig. 3a, b and Table 1). Interestingly, despite the highest catalytic activity (*i.e.*, lowest R_{ct}), $BiVO_4$/Co/N-TAGQD exhibited the highest A/R ratio. These results suggest that the ultrathin Co/N-TAGQD layers can also act as hole-storage layers as well as improve the charge separation efficiency and catalytic activity with a suitable band position (Fig. S19, S20,† and Scheme 2).

According to previous literature, the most GQD-modified photoanode needed complicated catalyst treatment due to the low adhesion property and poor catalytic activity of GQDs. In contrast, as-prepared polyphenol-derived GQDs can address the aforementioned issues. First, the strong adhesion of the ultrathin and uniform nanocarbon layer results in the enhanced stability of photoanodes. Second, both charge separation and charge transfer ability can be improved by the efficient and simple metal–phenolate–carbon complex within the nanocarbon layer. Third, we successfully demonstrate the multifunctional role of the nanocarbon layer through a systematic analysis.

Conclusions

In summary, we report that the ultrathin and stable layers can be formed on a model $BiVO_4$ photoanode and significantly improve the PEC performance for solar water oxidation. Abundant functional groups in N-TAGQDs, such as phenolic, carboxylic, and pyrrolic N groups, allowed the deposition of the uniform, ultrathin, and stable nanocarbon layers on photoanodes by a simple dipping method through strong complexation. We found that the ultrathin layers of N-TAGQDs and Co^{2+} ions can have multifunctional roles for efficient PEC water oxidation, such as improving charge separation, hole storage, and catalytic activity. As a result, $BiVO_4$/Co/N-TAGQD photoanodes showed excellent PEC performance and stability without the need for complex surface modifications. We believe that our approaches can be combined with various types of (photo) electrodes for energy applications.

Author contributions

Y. C. and S. B. contributed equally to this work. J. R. conceived the concept. Y. C. and B.-S. K. designed graphene quantum dots

and Y. C. synthesized and analyzed graphene quantum dots. Y. C. and S. B. performed photoelectrochemical experiments, and S. B. analyzed the data. Y. C., S. B., B.-S. K., and J. R. wrote the manuscript. All authors discussed the results and participated in writing the manuscript.

Conflicts of interest

There are no conflicts to declare.

Acknowledgements

This work was supported by the Basic Science Research Program (2021R1A2C2013684), the Technology Development Program to Solve Climate Changes (2019M1A2A2065616) and the Nano-Material Technology Development Program (2017M3A7B4052798, 2017M3A7B4052802, and 2021M3H4A1A03051390) through the National Research Foundation of Korea (NRF) funded by the Ministry of Science and ICT or Korea. This study was also supported by the Basic Science Research Programs (2018R1D1A1A02046918, 2020R1I1A1A01057924, and 2020R1A6A3A13077458) through the NRF funded by the Ministry of Education of Korea.

Notes and references

1 M. G. Walter, E. L. Warren, J. R. McKone, S. W. Boettcher, Q. Mi, E. A. Santori and N. S. Lewis, *Chem. Rev.*, 2010, **110**, 6446–6473.
2 S. Bae, J. E. Jang, H. W. Lee and J. Ryu, *Eur. J. Inorg. Chem.*, 2019, **2019**, 2040–2057.
3 J. H. Kim, D. Hansora, P. Sharma, J. W. Jang and J. S. Lee, *Chem. Soc. Rev.*, 2019, **48**, 1908–1971.
4 V. Kumaravel, J. Bartlett and S. C. Pillai, *ACS Energy Lett.*, 2020, **5**, 486–519.
5 B. H. R. Suryanto, H. L. Du, D. B. Wang, J. Chen, A. N. Simonov and D. R. MacFarlane, *Nat. Catal.*, 2019, **2**, 290–296.
6 J. Ryu, S. H. Lee, D. H. Nam and C. B. Park, *Adv. Mater.*, 2011, **23**, 1883–1888.
7 B. Klahr, S. Gimenez, F. Fabregat-Santiago, T. Hamann and J. Bisquert, *J. Am. Chem. Soc.*, 2012, **134**, 4294–4302.
8 Y. Choi, D. Jeon, Y. Choi, D. Kim, N. Kim, M. Gu, S. Bae, T. Lee, H. W. Lee, B. S. Kim and J. Ryu, *ACS Nano*, 2019, **13**, 467–475.
9 T. W. Kim and K. S. Choi, *Science*, 2014, **343**, 990–994.
10 S. Bae, H. Kim, D. Jeon and J. Ryu, *ACS Appl. Mater. Interfaces*, 2019, **11**, 7990–7999.
11 H. H. Sun, W. Hua, Y. Y. Li and J. G. Wang, *ACS Sustainable Chem. Eng.*, 2020, **8**, 12637–12645.
12 D. Jeon, N. Kim, S. Bae, Y. Han and J. Ryu, *ACS Appl. Mater. Interfaces*, 2018, **10**, 8036–8044.
13 F. F. Abdi, L. Han, A. H. Smets, M. Zeman, B. Dam and R. Van De Krol, *Nat. Commun.*, 2013, **4**, 1–7.
14 L. Wang, W. Si, Y. Tong, F. Hou, D. Pergolesi, J. Hou, T. Lippert, S. X. Dou and J. Liang, *Carbon Energy*, 2020, **2**, 223–250.
15 J. N. Tiwari, A. N. Singh, S. Sultan and K. S. Kim, *Adv. Energy Mater.*, 2020, **10**, 2000280.
16 A. Cadranel, J. T. Margraf, V. Strauss, T. Clark and D. M. Guldi, *Acc. Chem. Res.*, 2019, **52**, 955–963.
17 Y. Choi, Y. Choi, O. H. Kwon and B. S. Kim, *Chem.–Asian J.*, 2018, **13**, 586–598.
18 R. Tang, S. Zhou, C. Li, R. Chen, L. Zhang, Z. Zhang and L. Yin, *Adv. Funct. Mater.*, 2020, **30**, 2000637.
19 G. Zeng, L. Hou, J. Zhang, J. Zhu, X. Yu, X. Fu, Y. Zhu and Y. Zhang, *ChemCatChem*, 2020, **12**, 3769–3775.
20 H. Chen, S. Wang, J. Wu, X. Zhang, J. Zhang, M. Lyu, B. Luo, G. Qian and L. Wang, *J. Mater. Chem. A*, 2020, **8**, 13231–13240.
21 G. A. M. Hutton, B. C. M. Martindale and E. Reisner, *Chem. Soc. Rev.*, 2017, **46**, 6111–6123.
22 Y. Choi, D. Jeon, Y. Choi, J. Ryu and B. S. Kim, *ACS Appl. Mater. Interfaces*, 2018, **10**, 13434–13441.
23 X. W. Lv, X. Xiao, M. L. Cao, Y. Bu, C. Q. Wang, M. K. Wang and Y. Shen, *Appl. Surf. Sci.*, 2018, **439**, 1065–1071.
24 K.-H. Ye, Z. Wang, J. Gu, S. Xiao, Y. Yuan, Y. Zhu, Y. Zhang, W. Mai and S. Yang, *Energy Environ. Sci.*, 2017, **10**, 772–779.
25 P. Luan, X. Zhang, Y. Zhang, Z. Li, U. Bach and J. Zhang, *ChemSusChem*, 2019, **12**, 1240–1245.
26 S. Alam, T. K. Sahu, D. Gogoi, N. R. Peela and M. Qureshi, *Sol. Energy*, 2020, **199**, 39–46.
27 C. Liu, Y. Qiu, F. Wang, L. Li, Q. Liang and Z. Chen, *Ceram. Int.*, 2017, **43**, 5329–5333.
28 X. Xie, Y. Yang, Y.-H. Xiao, X. Huang, Q. Shi and W.-D. Zhang, *Int. J. Hydrogen Energy*, 2018, **43**, 6954–6962.
29 Z. Zeng, T. Li, Y.-B. Li, X.-C. Dai, M.-H. Huang, Y. He, G. Xiao and F.-X. Xiao, *J. Mater. Chem. A*, 2018, **6**, 24686–24692.
30 K.-H. Ye, H. Li, D. Huang, S. Xiao, W. Qiu, M. Li, Y. Hu, W. Mai, H. Ji and S. Yang, *Nat. Commun.*, 2019, **10**, 1–9.
31 Y. Choi, B. Kang, J. Lee, S. Kim, G. T. Kim, H. Kang, B. R. Lee, H. Kim, S. H. Shim, G. Lee, O. H. Kwon and B. S. Kim, *Chem. Mater.*, 2016, **28**, 6840–6847.
32 H. A. Lee, E. Park and H. Lee, *Adv. Mater.*, 2020, **32**, 1907505.
33 H. Ejima, J. J. Richardson, K. Liang, J. P. Best, M. P. van Koeverden, G. K. Such, J. Cui and F. Caruso, *Science*, 2013, **341**, 154–157.
34 M. A. Rahim, H. Ejima, K. L. Cho, K. Kempe, M. Müllner, J. P. Best and F. Caruso, *Chem. Mater.*, 2014, **26**, 1645–1653.
35 G. Zhang, G. Kim and W. Choi, *Energy Environ. Sci.*, 2014, **7**, 954–966.
36 Y. Shi, Y. Yu, Y. Liang, Y. Du and B. Zhang, *Angew. Chem., Int. Ed.*, 2019, **58**, 3769–3773.
37 Y. Wang, S. Chen, S. Zhao, Q. Chen and J. Zhang, *J. Mater. Chem. A*, 2020, **8**, 15845–15852.
38 T. Tian, C. Z. Dong, X. M. Liang, M. Yue and Y. Ding, *J. Catal.*, 2019, **377**, 684–691.
39 Y. M. Shi, Y. F. Yu, Y. Yu, Y. Huang, B. H. Zhao and B. Zhang, *ACS Energy Lett.*, 2018, **3**, 1648–1654.
40 F. Liu, X. He, H. Chen, J. Zhang, H. Zhang and Z. Wang, *Nat. Commun.*, 2015, **6**, 8003.
41 I. P. Hamilton, B. Li, X. Yan and L. S. Li, *Nano Lett.*, 2011, **11**, 1524–1529.

42 P. Wang, Y. Ren, R. Wang, P. Zhang, M. Ding, C. Li, D. Zhao, Z. Qian, Z. Zhang, L. Zhang and L. Yin, *Nat. Commun.*, 2020, **11**, 1576.
43 D. Hong, Y. Choi, J. Ryu, J. Mun, W. Choi, M. Park, Y. Lee, N.-S. Choi, G. Lee and B.-S. Kim, *J. Mater. Chem. A*, 2019, **7**, 20325–20334.
44 M. R. Huang, Z. W. Huang and H. W. Zhu, *Nano Energy*, 2020, **70**, 104487.
45 F. Malara, A. Minguzzi, M. Marelli, S. Morandi, R. Psaro, V. Dal Santo and A. Naldoni, *ACS Catal.*, 2015, **5**, 5292–5300.
46 G. M. Carroll and D. R. Gamelin, *J. Mater. Chem. A*, 2016, **4**, 2986–2994.
47 S. Bae, D. Kim, H. Kim, M. Gu, J. Ryu and B. S. Kim, *Adv. Funct. Mater.*, 2020, **30**, 1908492.
48 H. Xu, D. Cheng, D. Cao and X. C. Zeng, *Nat. Catal.*, 2018, **1**, 339–348.
49 B. Jin, Y. Cho, Y. Zhang, D. H. Chun, P. Li, K. Zhang, K.-S. Lee and J. H. Park, *Nano Energy*, 2019, **66**, 104110.
50 Q. Sun, T. Cheng, Z. Liu and L. Qi, *Appl. Catal., B*, 2020, **277**, 119189.
51 S. Byun, B. Kim, S. Jeon and B. Shin, *J. Mater. Chem. A*, 2017, **5**, 6905–6913.
52 S. Byun, G. Jung, Y. Shi, M. Lanza and B. Shin, *Adv. Funct. Mater.*, 2020, **30**, 1806662.